Numerical study of charge transport layers in inverted ternary organic photovoltaic cells

Vincent Magnin, Kekeli N'konou

EPJ Photovoltaics **15**, 29 (2024)

https://doi.org/10.1051/epjpv/2024024

Available online at:
www.epj-pv.org

ORIGINAL ARTICLE OPEN ACCESS

Numerical study of charge transport layers in inverted ternary organic photovoltaic cells

Vincent Magnin* and Kekeli N'Konou**

University Lille, CNRS, Centrale Lille, University Polytechnique Hauts-de-France, Junia-ISEN, UMR 8520 – IEMN, 59000 Lille, France

Received: 17 May 2024 / Accepted: 17 July 2024

Abstract. This study investigates the crucial role of charge transport layers in enhancing the performance of inverted organic photovoltaic cells (OPVs) through advanced numerical simulations using OghmaNano software. OPVs offer distinct advantages, including lightweight, flexibility, and potential cost-effectiveness compared to traditional silicon-based counterparts, making them pivotal for sustainable energy solutions. We evaluate the efficiency of inverted (iOPVs) employing binary (PM6:L8-BO) and ternary (PM6:D18:L8-BO) active layers, utilizing electron transport layers (ETLs) including ZnO, TiO_2, and SnO_2, and hole transport layers (HTLs) such as MoO_3, PEDOT, and WO_3. Results highlight ZnO with a 15 nm-thick layer combined with MoO_3 HTL achieving an impressive efficiency of 18.89% in ternary devices, demonstrating the effectiveness of organic materials and ternary blends. The study demonstrates that TiO_2 or SnO_2 ETLs can compete effectively with ZnO ETLs, particularly when used at thinner thicknesses, and offers alternative fabrication methods. It suggests that employing thin ETL layers (15 ± 2 nm) could significantly enhance the performance of iOPV devices. Simulations are crucial for optimizing iOPV device configurations with thin ETL layers, enabling rapid prototyping and cost-effective exploration of material combinations and device architectures. These layers play a critical role in balancing charge carrier generation and transport efficiency, collectively maximizing device performance. Overall, the study underscores the pivotal role of simulations and optimized layer thicknesses in advancing OPV technology by refining manufacturing processes and accelerating the adoption of OPVs for sustainable energy solutions.

Keywords: Inverted organic photovoltaic cells / thin electron transport layers / hole transport layers / ternary strategy

1 Introduction

The development of organic photovoltaic cells (OPVs) is garnering a great deal of attention in both academic and industrial communities, driven by their distinct advantages over conventional inorganic solar cells. One significant benefit lies in their versatility, allowing OPVs to be manufactured on lightweight and flexible materials. This characteristic makes them appropriate for use in portable electronics, wearable devices, building-integrated photovoltaics, and as innovative energy sources for outdoor and indoor applications [1–4]. This flexibility is enabled by organic materials and manufacturing techniques such as printing and roll-to-roll processing, which are more cost-effective and less energy-intensive than the high-vacuum methods required for inorganic solar cells such as CIGS, Si, CdTe, etc. Furthermore, organic materials in OPVs can be precisely tuned to absorb specific wavelengths of light, potentially enhancing efficiency and enabling the development of multi-junction cells capable of capturing a wider spectrum of sunlight. From an ecological perspective, OPVs typically utilize non-toxic materials and avoid rare elements, offering a more environmentally friendly alternative to certain inorganic technologies that rely on hazardous substances like cadmium [5,6]. The power conversion efficiency (PCE) of OPVs has been further enhanced owing to the synthesis of novel active materials and the design of new device architectures. The OPV device typically consists of a bottom transparent conductive electrode, a photoactive layer sandwiched between an electron transporting layer (ETL) and hole transporting layer (HTL), and a top metal electrode. The photoactive layer is generally composed of two organic semiconductors, one electron donor (D), and one electron acceptor (A). This photo-active layer converts absorbed photons into charge carriers, which can be collected. The working principle of OPVs begins with the absorption of light by organic

* e-mail: vincent.magnin@univ-lille.fr
** e-mail: kekeli.nkonou@junia.com

materials in the active layer, creating excitons (bound electron-hole pairs). These excitons then diffuse to the D/A interface, which must be within a few nanometers due to their short diffusion lengths. At this interface, the excitons dissociate into free electrons and holes, with electrons moving to the acceptor material while holes remain in the donor material. Subsequently, the free electrons and holes travel through the acceptor and donor materials to their respective electrodes. Finally, in the conventional device structure, the electrons are collected at the cathode and the holes at the anode, whereas in the inverted device structure, this process is reversed. To achieve efficient charge collection, the work functions (WF) of both electrodes, the anode, and cathode, should align with the highest occupied molecular orbital (HOMO) of the donor and the lowest unoccupied molecular orbital (LUMO) of the acceptor, respectively [7]. Furthermore, it is crucial to effectively reduce charge recombination to maintain device efficiency. Despite their advantages, OPVs face challenges such as lower efficiency and stability compared to inorganic counterparts. In conventional device structures, the ETL layer like PEDOT:PSS (poly(3,4-ethylenedioxythiophene)-poly(styrenesulfonate)), can corrode the ITO electrode. Moreover, during vacuum evaporation deposition, the top metal electrode is prone to oxidation in air, forming micropores. This permits oxygen and moisture to penetrate the photoactive layer, speeding up the degradation of the underlying polymer. These factors collectively contribute to the decreased stability of solar devices [8]. To address these challenges and enhance device stability, inverted (ETL-active layer-HTL) device structures have been developed. In a standard device structure, holes are injected into transparent indium-tin-oxide (ITO), and electrons are injected into the counter electrode, such as aluminum. Conversely, in an inverted device structure, electrons are injected into the ITO, and holes are collected by the top electrode, which can be a less air-sensitive, high-work-function metal like silver (Ag) or gold (Au). In comparison to standard configurations, inverted OPVs (iOPVs) are preferred for their enhanced stability and longer operational lifetimes. This improvement is primarily due to better protection of the active layer against degradation and increased stability of the electrodes [9,10]. Previous studies [11–13] have shown the importance of ETL design on interfacial contacts, electron extraction efficiency, device stability, and device lifetime. Various strategies have been explored to enhance the performance of iOPV devices. Low work-function metal oxides such as zinc oxide (ZnO), tin oxide (SnO_2), and titanium dioxide (TiO_2) are commonly chosen for their inherent properties like ultraviolet (UV) and visible (Vis) light photons, stability, ease of preparation, and potential to modify optical energy band structures, making them effective materials for the ETL [14–19]. These metal oxides enhance iOPV performance not only due to their intrinsic properties but also because of their specific WF and band alignments, which critically influence OPV device efficiency, stability, and overall functionality. The choice of ETL and HTL materials significantly impacts device performance; for ETLs like ZnO, SnO_2, and TiO_2 in iOPVs, ZnO (WF 4.3–4.4 eV) excels with high electron mobility, transparency, and compatibility with organic donor LUMO levels, facilitating efficient charge separation. Similarly, SnO_2 (WF ∼4.5 eV) provides good mobility, UV stability, and transparency, while TiO_2 (WF 4.2–4.4 eV) is noted for its photocatalytic activity and stability, facilitating effective electron transfer. Investigating HTLs such as MoO_3 (WF 5.3–5.7 eV), WO_3 (WF 4.7–5.0 eV), and PEDOT:PSS (WF ∼5.0 eV) highlights their roles in efficient hole extraction and transport by aligning well with the HOMO levels of organic donors [20,21]. Proper alignment of ETL conduction bands with donor LUMOs and HTL HOMOs with acceptor HOMOs is crucial for minimizing recombination losses and optimizing charge separation efficiency, thereby enhancing overall device performance and stability. Materials with suitable WFs also mitigate charge accumulation at interfaces, ensuring long-term device reliability and maximizing power conversion efficiency. This comprehensive discussion underscores the critical role of material properties in designing advanced OPVs and justifies the selection of specific materials in this study. Moreover, several successful D/A materials are employed to construct high-performance OPV devices. For instance, the polymer donor PM6 is demonstrated to be one of the most effective materials for matching different acceptors, achieving a PCE now over 20% for single-junction devices [22,23]. Among different attempts for improving PCEs, ternary blend systems, which typically include one donor and two acceptors or two donors and one acceptor, have achieved significant progress toward their optimal performance owing to the presence of the third component [24–26]. The third component's light absorption spectrum is often complementary to that of the light-harvesting polymer, and it is included in the donor/acceptor binary blend. The existence of the third component, when combined with the other two components, might result in the formation of an energy level cascade for charge transfer, as well as the development of film morphology [27]. Nevertheless, the appropriate selection of OPV transporting layer materials and thickness is vital for improving their performance, such as efficiency and stability. Utilizing HTL like MoO_3, vanadium pentoxide, nickel oxide, WO_3, and PEDOT:PSS has been common, yet their impact on iOPV performance, especially in binary and ternary blends, remains underexplored for optimizing effective organic thin films in solar applications. In this study, we chose to employ numerical simulations because they allow for rapid prototyping, cost-effective exploration of different material combinations and device architectures, and offer insights into the underlying physical processes without requiring extensive experimental trials. Our numerical study aims to evaluate binary and ternary iOPVs by adjusting ETL thicknesses and experimenting with different HTL materials to find optimal configurations, highlighting ZnO, SnO_2, and TiO_2 for ETLs, and MoO_3, WO_3, and PEDOT:PSS for HTLs.

2 Simulation parameters

To predict the electrical parameters including open-circuit voltage (V_{oc}), short-circuit current density (J_{sc}), fill factor (FF), and PCE of the iOPV devices, we employed OghmaNano 8.0.032 simulation software. Formerly known as GPVDM (General-purpose Photovoltaic Device Model), OghmaNano, exclusively available for Microsoft Windows, is a free software tool utilized for simulating optoelectronic devices including perovskites [28], and organic light-emitting diodes [29]. It has been extensively used to thoroughly evaluate OPV devices [30–35]. In OghmaNano, understanding exciton properties is essential for accurately simulating organic OPV devices. The exciton binding energy, which dictates charge generation and separation efficiency, along with exciton diffusion length, governing how far excitons travel before recombining, significantly influences charge separation efficiency. Moreover, the exciton lifetime plays a critical role in determining the probability of exciton diffusion to the donor-acceptor interface during charge separation. OghmaNano intricately integrates these properties to achieve precise simulations of OPV device behavior. Furthermore, the exciton generation rate, which quantifies exciton production per unit volume per unit time upon light absorption, directly affects photocurrent and device performance. Additionally, the energy levels of D/A materials, including HOMO and LUMO levels, influence the exciton dissociation process and the driving force for charge separation. When employing an effective medium model in OghmaNano, these properties are harmoniously incorporated into simulations to offer a comprehensive and accurate portrayal of OPV behavior. This modeling approach averages the properties of composite materials to simulate exciton formation, movement, and dissociation within mixed organic layers, facilitating detailed and realistic predictions of OPV device performance. In addition, OghmaNano incorporates critical material properties including permittivity, mobility coefficients for charge carriers, band gap energies, and electron affinities. These properties play a crucial role in accurately simulating the behavior of optoelectronic materials in devices such as OPVs and OLEDs, thereby facilitating the optimization of device performance and efficiency [36]. OghmaNano uses a finite difference numerical method to solve the drift-diffusion model, accurately modeling transport and recombination processes within OPV devices. It incorporates Shockley-Read-Hall dynamics and accurately captures carrier transport and recombination through Poisson and continuity equations. The transfer matrix method handles optical effects, while Poisson's equation models electrostatic effects. This approach enables accurate simulation of carrier distribution in position and energy spaces, facilitating the generation of J-V characteristics and determining band gaps based on the HOMO and LUMO levels of donor and acceptor materials. The D/A blend is treated as an effective medium where the properties of the organic components are homogenized. The charge separation is facilitated by the built-in electric field provided by the contacts, rather than explicitly modeling exciton dynamics and dissociation. Here, we outlined the carrier transport model in OghmaNano, but comprehensive operational details of the model can be found in the literature [36–38]. This software uses the effective medium approximation to simulate carrier transport in the OPV. In this approach, the band gap (E_g) is defined as the difference between the LUMO of the donor and the HOMO of the acceptor. The potential distribution (ϕ) within the device is calculated by solving the Poisson equation (Eq. (1)).

$$\frac{d}{dx}\cdot\left(\varepsilon_0\varepsilon_r\frac{d\Phi}{dx}\right)=q\left(n_{free}-p_{free}+n_{trap}-p_{trap}\right) \tag{1}$$

where ε_0 is the permittivity of free space, ε_r represents the relative permittivity of the active layer, and q is the elementary charge. The densities of free electrons and holes are represented as n_{free} and p_{free}, while those of trapped carriers are denoted by n_{trap} and p_{trap}. To calculate the electron current density (J_n) and hole current density (J_p), the continuity equations (Eqs. (2) and (3)) are used. These equations consider the total carrier densities (both free and trapped) of electrons (n) and holes (p), the generation rate of free charge carriers (G), and the recombination rates of electrons (R_n) and holes (R_p).

$$\frac{dJ_n}{dx}=q\left(R_n-G+\frac{\partial n}{\partial t}\right) \tag{2}$$

$$\frac{dJ_p}{dx}=-q\left(R_p-G+\frac{\partial p}{\partial t}\right). \tag{3}$$

The free carriers are assumed to adhere to Maxwell–Boltzmann statistics. The mobility edges for free electrons and holes, defined as E_{LUMO} and E_{HOMO} respectively, are given by:

$$E_{LUMO}=-(\chi+q\Phi) \tag{4}$$

$$E_{HOMO}=-\left(\chi+E_g+q\Phi\right) \tag{5}$$

where χ is the electron affinity of the active layer.

Finally, equations (6) and (7), which represent the momentum conservation equations (drift-diffusion equations) for electrons and holes, are solved:

$$J_n=q\mu_e n\frac{\partial E_{LUMO}}{\partial x}+qD_n\frac{\partial n}{\partial x} \tag{6}$$

$$J_p=q\mu_h p\frac{\partial E_{HOMO}}{\partial x}-qD_p\frac{\partial p}{\partial x} \tag{7}$$

where μ_e and μ_h are the mobility coefficients for electrons and holes, while D_n and D_p denote the diffusion coefficients for electrons and holes, respectively. In OghmaNano software, the structure calibration is performed through systematic steps to ensure precise device performance simulations. The process begins by selecting a configuration from the software's extensive library of various organic semiconductor devices. Users then customize simulation parameters in a dedicated window, adjusting details such as materials, layer thicknesses, and operational settings

Table 1. The primary input parameters used in the Oghmanano simulation for the active layers.

Electrical parameter	Binary	Ternary	Unit
Free carriers			
Electron mobility	1.50e-07	1.49e-07	$m^2V^{-1}s^{-1}$
Hole mobility	1.15e-07	1.42e-07	$m^2V^{-1}s^{-1}$
Effective density of free electron states	1e26	1e26	m^{-3}
Effective density of free hole states	1e26	1e26	m^{-3}
Recombination rate constant	1.77e-17	1.15e-17	m^3s^{-1}
Equilibrium SRH traps			
n_1, p_1	1e20	1e20	m^{-3}
τ_n, τ_p	1e-15	1e-15	s^{-1}
Non-equilibrium SRH traps			
Free electron to trapped electron	1e-15	1e-15	m^{-2}
Trapped electron to free hole	1e-20	1e-20	m^{-2}
Trapped hole to free electron	1e-20	1e-20	m^{-2}
Free hole to trapped hole	1e-15	1e-15	m^{-3}
Electrostatics			
χ	4.2	4.2	eV
E_g	1.28	1.29	eV
Relative permittivity	3.0	3.0	au
Excitons			
Scattering length	4.221e-8	4.272e-8	m
Lifetime	3.6e-10	3.6e-10	s^{-1}
k_{pl}	2.78e9	2.78e9	s^{-1}
k_{dis}	2.17e12	1.96e12	s^{-1}

like temperature and light intensity. Once these parameters are set, the simulation is executed, generating key performance metrics, including V_{oc}, J_{sc}, FF, and PCE. The results are analyzed and compared with experimental data to validate accuracy. Iterative adjustments, guided by the literature and experimental insights, are made to refine the model for a more accurate representation of the OPV device. The entire calibration process is well-documented in the literature [36,37], providing a reference for users to replicate the steps. Critical physical parameters used in the simulations, such as charge mobility, recombination rates, and optical properties, are detailed and summarized in Table 1 (see also Fig. S1 in the Supplementary information). By following these steps, OghmaNano ensures accurate modeling of OPV devices, resulting in reliable and insightful simulation outcomes.

In comparison to other computational methods such as molecular dynamics (MD), quantum chemical calculations, and Monte Carlo (MC) simulations, OghmaNano provides a balanced approach that combines accuracy with computational efficiency. This makes it particularly suitable for modeling disordered materials like organic semiconductors. While MD simulations provide detailed atomistic interactions and dynamics, they are computationally intensive. Quantum chemical calculations accurately determine charge transfer rates but are limited by scalability. MC simulations model charge transport over longer timescales and larger systems.

Figure 1a shows the chemical structures of L8-BO (2,2'-((2Z,2'Z)-((12,13-bis(2-ethylhexyl)-3,9-(2-butyloctyl)-12,13-dihydro-[1,2,5]thiadiazolo[3,4-e]thieno[2,"3":4',5'] thieno[2',3':4,5]pyrrolo[3,2g]thieno [2',3': 4,5] thieno[3,2-b] indole-2,10-diyl)bis(methanylylidene))bis(5,6-difluoro-3-oxo-2,3-dihydro-1H-indene-2,1-diylidene))dimalononitrile as non-fullerene acceptors, D18 (Poly[(2,6-(4,8-bis(5-(2-ethylhexyl-3-fluoro)thiophen-2-yl)-benzo[1,2-b:4,5-b'] dithiophene))-alt-5,5'-(5,8-bis(4-(2-butyloctyl)thiophen-2-yl)dithieno[3',2':3,4;2",3":5,6]benzo[1,2-c][1,2,5] thiadiazole)]), and PM6 (Poly[(2,6-(4,8-bis(5-(2-ethylhexyl-3-fluoro)thiophen-2-yl)-benzo[1,2-b:4,5b']dithiophene))-alt-(5,5-(1',3'-di-2-thienyl-5',7'-bis(2-ethylhexyl) benzo [1',2'-c:4',5'-c']dithiophene-4,8-dione)]) used as polymer donors, utilized in this work to form the binary and ternary blends. Figure 1b depicts the schematic energy levels of all functional layers in the iOPVs, indicating a gradient energy alignment for charge transport. Excitons may be created inside the active layer when exposed to sunlight, and they then diffuse to the donor-acceptor interfaces. The charges will then be separated at the donor-acceptor interfaces and carried to the transporting layers, with electrons to ETL and holes to HTL.

Here, we simulated the iOPV devices using different configurations, where each HTL material has three possible configurations. Figure 2 shows the structure of simulated iOPVs with the structure of ITO/ETL/Active layer/HTL/Ag where the ETL materials used are ZnO, SnO_2, and TiO_2

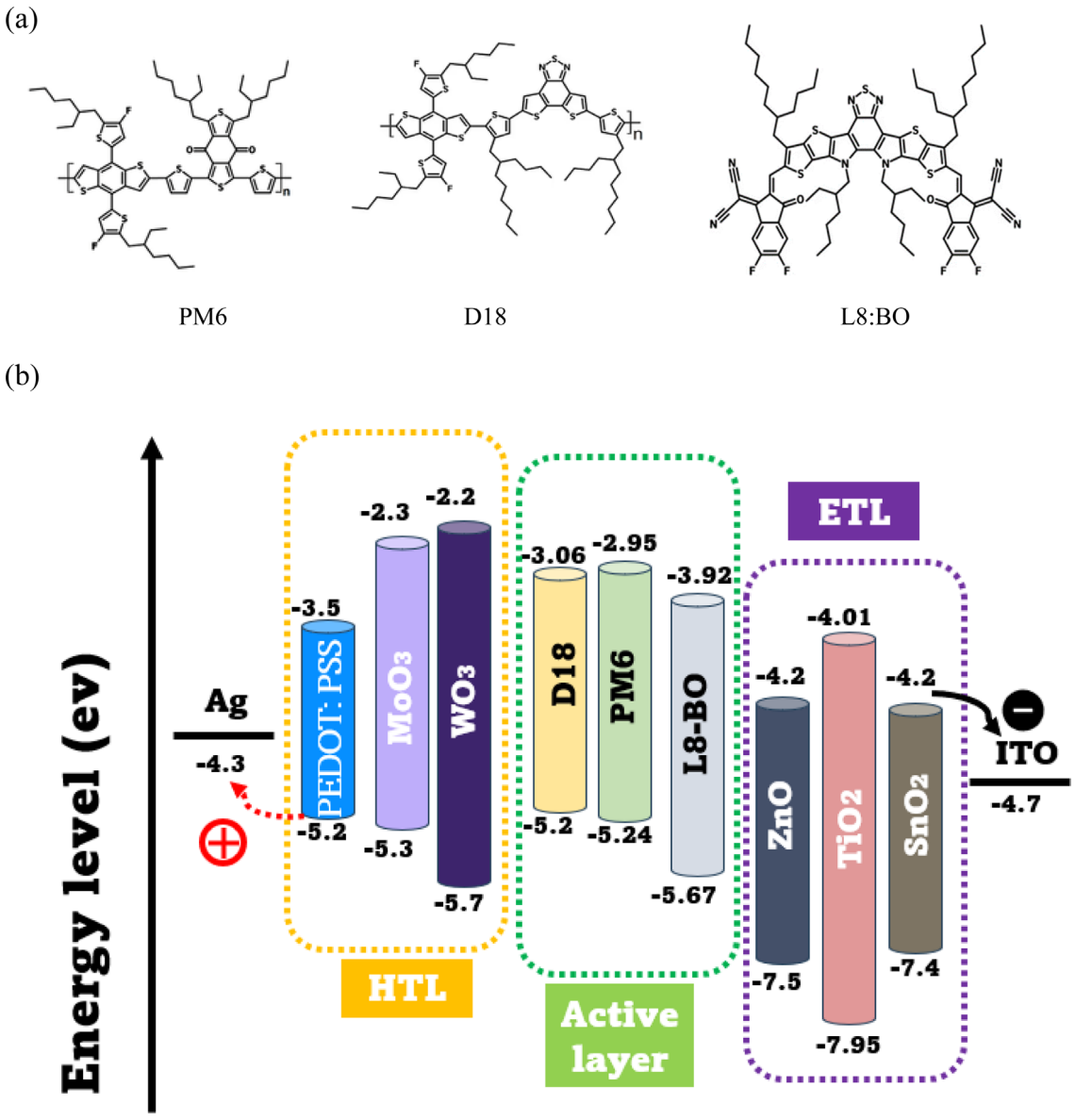

Fig. 1. a) Molecular structures of active layer materials (PM6, D18, and L8-BO); b) Energy level diagram that includes the HOMO levels, LUMO levels, and work function of the materials utilized in this work.

and the HTL materials chosen here are WO_3, MoO_3, and PEDOT:PSS. Table 2 lists the band parameters of all functional layers and Figure 1b shows the energy diagram for each cell component. The optical constants of PM6:L8-BO and PM6:D18:L8-BO are taken from the literature [42], and the Ag, MoO_3, ZnO, ITO, TiO_2, and SiO_2 optical constants are obtained from the reference website https://refractiveindex.info/.

It should be noted that the initial results produced by the OghmaNano software may show slight, transient oscillations due to the mesh discretization. To improve the readability and facilitate comparisons among different materials, we opted to fit the data with fourth-degree polynomials as presented in Figure S2 (see the Supplementary information).

3 Results and discussion

3.1 Influence of active layer thickness on the photovoltaic performance of iOPVs based on binary and ternary blends

The optimization of the active layer thickness is pivotal in determining the photovoltaic performance of iOPVs employing binary and ternary blends. This parameter significantly influences the efficiency of energy conversion processes essential to OPV technology. OPVs convert energy through a series of steps, beginning with light absorption that generates excitons. These excitons then move to the D/A interface, where they split into free charge carriers. These carriers are transported to their respective

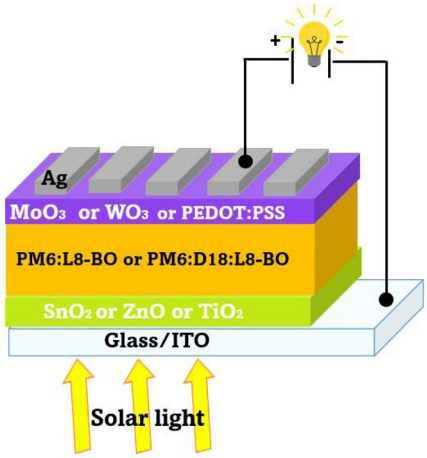

Fig. 2. Schematic illustration of the iOPV-based binary (PM6:L8-BO) and ternary (PM6:D18:L8-BO) blends with various ETL materials (SnO_2, ZnO or TiO_2) as well as different HTL materials (MoO_3, WO_3 or PEDOT:PSS) used in this work.

electrodes, producing photocurrent and enhancing the overall efficiency of the device. Therefore, optimizing the thickness of binary and ternary iOPV configurations is essential to maximize light absorption, exciton dissociation, and charge carrier transport efficiency. To achieve this, we initially simulated devices with varying active layer thicknesses ranging from 80 to 200 nm, incrementally increasing by 1 nm steps. The iOPV structure comprises 100 nm-thick indium tin oxide (ITO) as a bottom transparent electrode, 40 nm-thick ZnO as an ETL, a photoactive layer (variable thickness), 10 nm-thick MoO_3 as a HTL, and 100 nm-thick silver (Ag) as a top electrode. Ag is chosen for its high conductivity, suitable work function for efficient electron collection, and high reflectivity, which enhances light trapping within the active layer. Moreover, Ag is more cost-effective than gold and offers better performance than Aluminum in terms of aligning with the work function of the ETL. The device was tested under standard illumination conditions of $1000\,W.m^{-2}$ (AM 1.5G illumination). To study the effect of the active-layer thickness on the photovoltaic performance of the devices, we first simulated binary (PM6:L8-BO) and ternary (PM6:D18:L8-BO) iOPVs with different active-layer thickness. We selected an active layer thickness ranging from 80 nm to 200 nm to align closely with experimental standards. This choice enhances light absorption efficiency and reduces recombination losses, as active layers typically achieve optimal performance within the range of 100 ± 20 nm for effective absorption. It should be noted that thicker layers (e.g., 600 nm) could increase recombination, while thinner layers (e.g., 50 nm) might not absorb sufficient light.

Figure 3 depicts the dependence of photovoltaic performance on active-layer thickness. Figure 3a shows that the PCE lowers swiftly as the active layer thickness increases due to a reduction in both V_{oc} and FF, implying that higher carrier recombination (due to increased thickness) significantly reduces charge collection efficiency in these thick-film devices. This confirms that the active layer thickness is a sensitive parameter for improving iOPV performance. Thus, the optimal thickness of the photoactive layer is 80 nm achieving a PCE of 17.94% with a V_{oc} of 0.865 V, and J_{sc} of $25.37\,mA \cdot cm^{-2}$ with a FF of 0.817, for binary OPVs, whereas the ternary devices exhibit a V_{oc} of 0.866 V and a higher J_{sc} of $26.29\ mA \cdot cm^{-2}$ with FF of 0.816, and a higher PCE of 18.59%. It is assumed that with the addition of the D18 polymer donor as a third component into the PM6:L8-BO host blend, the resultant PCE can be enhanced due to increased photovoltaic parameters, mainly the J_{sc}. Zhu et al. [42] experimentally demonstrated that PM6:D18:L8-BO based on ternary devices fabricated with the standard configuration outperforms PM6:L8-BO-based binary devices due to efficient exciton diffusion and suppressed recombination, leading to increased exciton dissociation yield and decreased free charge recombination in ternary blends. This conclusion aligns with findings from experiments, which emphasize the enhancement of ternary-based iOPV compared to binary iOPV [44–46].

3.2 Influence of the MoO_3 HTL material in iOPVs based on binary and ternary blends with three ETL materials

MoO_3 is recognized for its potential as a solution-processable material for the HTL in organic electronic devices, with electrical properties that facilitate charge injection and extraction. It represents a credible alternative to PEDOT:PSS which presents some limitations owing to its hydrophilic and acidic characteristics [47,48]. To study the influence of the thickness of three ETL materials on the performance of iOPVs, we employed three metal oxides SnO_2, ZnO, and TiO_2. Figure 4a shows a schematic illustration of an iOPV structure with three ETLs, and MoO_3 as HTL. The iOPV structure consists of 150 nm-thick ITO/ETL/80 nm-thick PM6:L8-BO or PM6:D18: L8-BO/10 nm-thick MoO_3/100 nm-thick Ag, and the ETL thickness is ranging from 5 to 40 nm. Figures 4b–4e depict the photovoltaic parameters of the binary and ternary devices versus the thicknesses of the various ETL materials.

The performance of ternary devices outperformed the binary devices regardless of the nature of ETL materials and thickness. This finding is consistent with our prior findings in Section 3.1, demonstrating the presence of D18 in the host blend improves photovoltaic properties by enhancing charge transfer, lowering recombination losses, and optimizing the morphology of the active layer. Among the six devices, the devices with SnO_2 ETL show the lowest performance by increasing the ETL thickness compared to the TiO_2 and ZnO-based iOPV devices. This can be attributed to the SnO_2 material's properties which could harm electronic mobility or energy level alignment with the active layer compared to TiO_2 and ZnO. The current density (J_{sc}) and overall performance of the device can be adversely affected by the mismatch, which can lead to an increase in serial resistance or inefficient load extraction. However, the FF and V_{oc} are quite similar for all devices regardless of ETL thicknesses. This suggests that the active layer has a greater influence on these two parameters than the ETL thickness, as well as the consistency of the active

Table 2. Bandgaps of each layer used in this study.

Materials	HOMO Level (eV)	LUMO Level (eV)	Band gaps (E_g) (eV)	References
PEDOT:PSS	−3.5	−5.2	1.7	[39]
MoO_3	−2.3	−5.3	3	[40]
WO_3	−2.2	−5.7	3.5	[41]
PM6	−3.06	−5.20	2.14	[42]
D18	−2.95	−5.24	2.29	
L8-BO	−3.92	−5.67	1.75	
ZnO	−4.2	−7.5	3.3	[40]
SnO_2	−4.01	−7.95	3.94	[43]
TiO_2	−4.2	−7.4	3.2	[41]

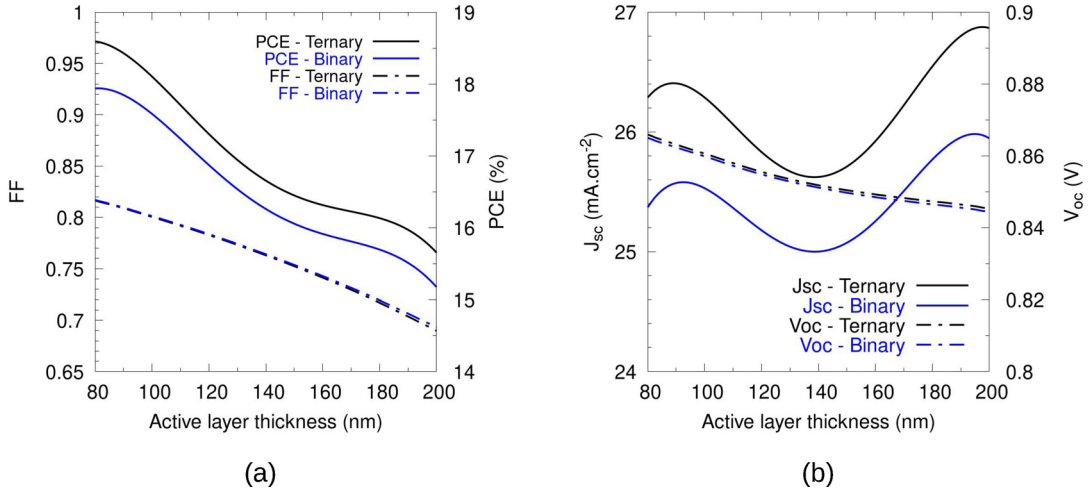

Fig. 3. Variations of iOPV based on binary and ternary devices' performance parameters with different thicknesses of photoactive layer: (a) FF and PCE; and (b) J_{sc} and V_{oc}. The blue color represents the photovoltaic parameters of binary devices and the black color is that of the ternary devices.

layer blend and MoO_3 HTL characteristics may be beneficial to stabilize FF and V_{oc} values across varied ETL thicknesses.

The best ternary iOPV delivers a maximum PCE of 18.89% along with a V_{oc} of 0.866 V, a higher J_{sc} (26.72 mA.cm^{-2}), and a FF of 0.8162 with 15 nm-thick ZnO ETL while the best binary iOPV with 17 nm-thick ZnO ETL exhibits a PCE of 18.28% with V_{oc} (0.865 V), J_{sc} (25.86 mA.cm^{-2}), and FF (0.817). In general, the observed device performance trends can be attributed to the interaction between active layer, ETL materials, and thicknesses as well as the overall device architecture, facilitated by a ternary blending approach. To better understand the effect of HTL material on the performance of iOPV devices, we changed the MoO_3 to WO_3 in the next section.

3.3 Influence of the WO_3 HTL material in iOPVs based on binary and ternary blends with three different ETL materials

HTL using WO_3 is favored due to its transparency, chemical stability, and high work function, which facilitate efficient hole extraction and transport in OPVs. These properties of WO_3 are particularly advantageous in enhancing device performance, especially under air-exposure conditions, as demonstrated by experimental studies. [49–51]

To examine the effect of the HTL WO_3 material on the performance of binary and ternary iOPVs, we tested SnO_2, ZnO, and TiO_2 as ETL materials with different thicknesses, as presented in Figure 5a. The thicknesses used for the different layers of the iOPV devices have been conserved and the MoO_3 HTL material has been substituted by WO_3. In terms of photovoltaic parameters enhancement, ternary devices with WO_3 HTL surpassed binary devices independent of ETL material or thickness (Figs. 5b–5e), indicating the evidence of ternary blend's benefits over binary blend under different configurations. Overall, the photovoltaic parameters results reveal that devices with SnO_2 ETL show the lowest performance as various ETL thickness increases, compared to TiO_2 and ZnO-based iOPV devices, aside from the FF and V_{oc} results, which demonstrate a negligible change (Fig. 5d). As mentioned in the previous section, the invariance of FF and V_{oc} values proves that these two parameters are not influenced by the thickness or material of the ETL layer.

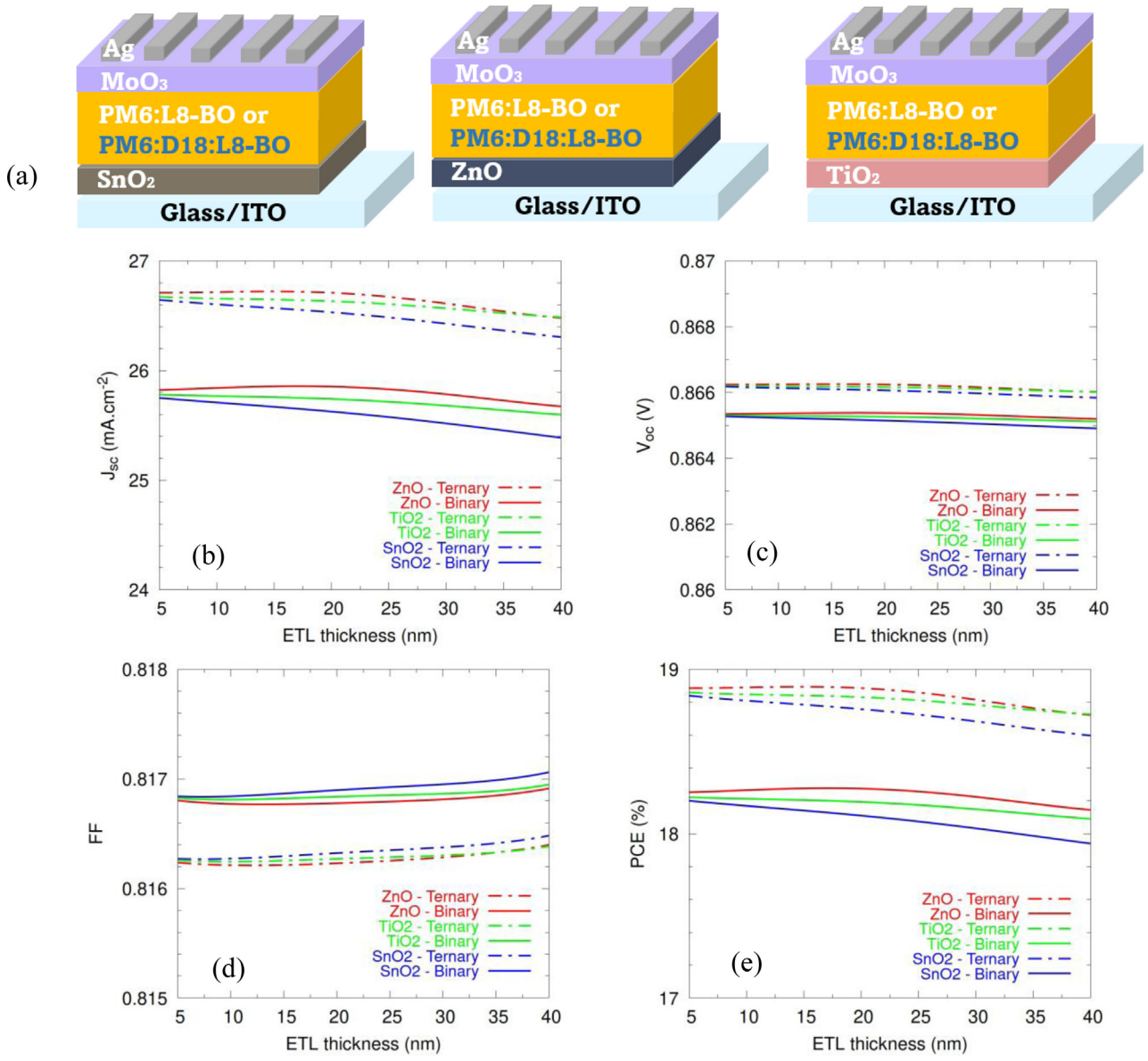

Fig. 4. (a) Schematic of the simulated iOPVs based on binary and ternary blends using different ETL materials with MoO_3 as HTL. Variations of iOPV device performance parameters with different thicknesses and materials of ETL: (b) J_{sc}, (c) V_{oc}, (d) FF, and (e) PCE.

The ternary iOPV with a 14 nm-thick ZnO ETL achieves a maximum PCE of 18.90% thanks to an improved J_{sc} of 26.73 mA.cm^{-2}. Similarly, the binary iOPV devices show the highest PCE of 18.28% with a ZnO ETL of 16 nm thickness, offering a J_{sc} of 25.87 mA.cm^{-2}, a FF of 0.8167, and a V_{oc} of 0.865 V. This outstanding performance is attributed to the efficient electron transport properties of ZnO and its well-aligned energy levels with the active layer, enabling effective charge extraction. Furthermore, iOPV devices with a WO_3 HTL achieve a PCE of 18.90% and a J_{sc} of 26.73 mA.cm^{-2}, which is comparable to iOPV devices with a MoO_3 HTL that have a PCE of 18.89% and a J_{sc} of 26.72 mA.cm^{-2}, with a similar ZnO ETL thickness and the same HTL thickness. This suggests that WO_3 is an efficient HTL material, offering competitive performance advantages similar to MoO_3 for specific configurations.

To illustrate that WO_3 and MoO_3 can serve as alternative HTL materials with properties comparable to PEDOT:PSS, we conducted a parallel study in the following section.

3.4 Influence of the PEDOT:PSS HTL material in iOPVs based on binary and ternary blends with three different ETL materials

The PEDOT:PSS is the cutting-edge, widely used interface material for efficiently transporting holes and blocking electrons, thereby minimizing leakage currents at the active layer/anode interface [52,53]. We previously employed PEDOT:PSS as HTL for the fabrication of iOPVs [53,54]. Additionally, the hydrophilic and acidic

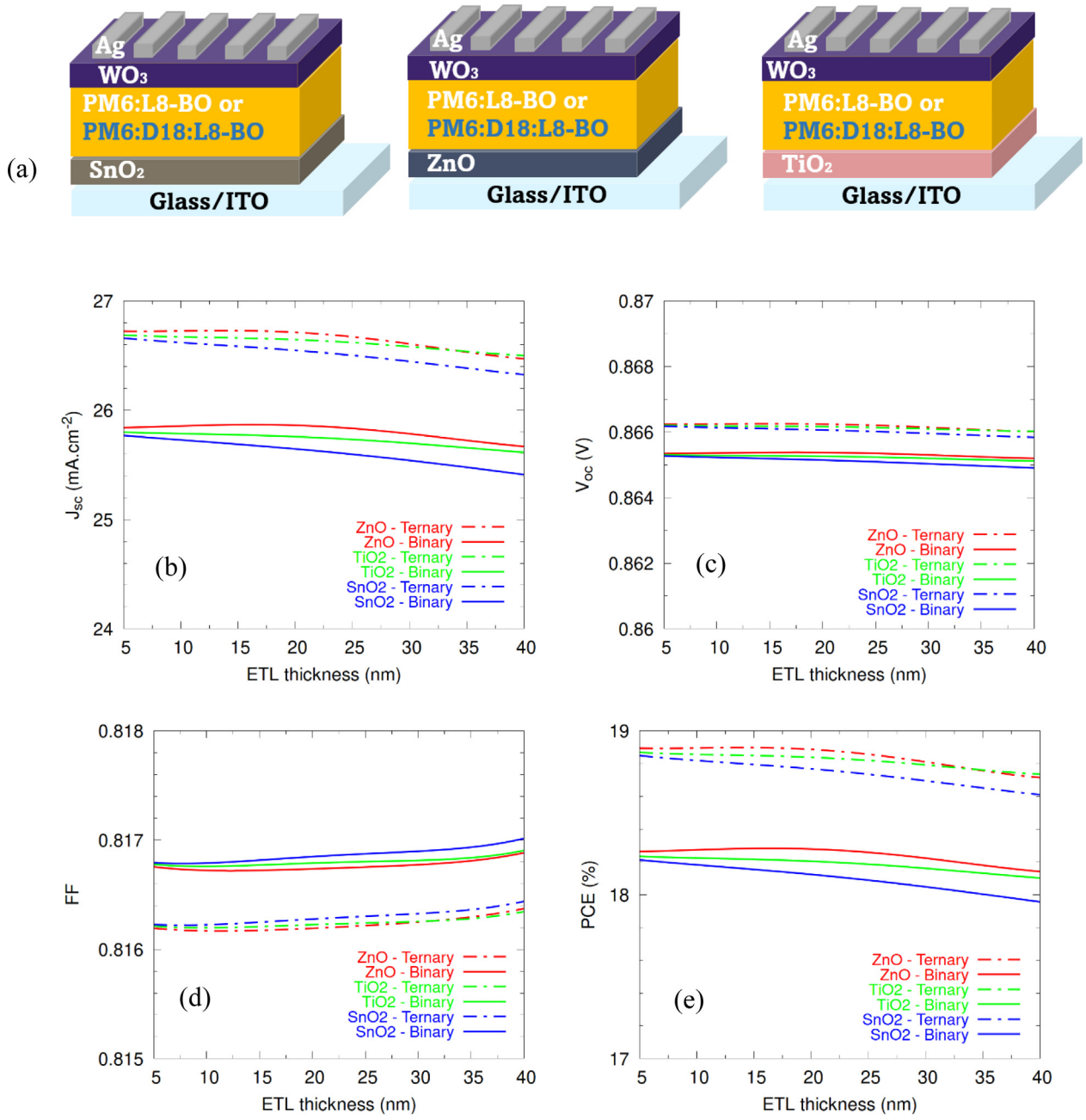

Fig. 5. (a) Schematic of the simulated iOPVs based on binary and ternary blends using different ETL materials with WO_3 as HTL. Variations of iOPV device performance parameters with different thicknesses and materials of ETL: (b) J_{sc}, (c) V_{oc}, (d) FF, and (e) PCE.

properties of PEDOT:PSS are highly hygroscopic, capable of absorbing moisture from the air. This characteristic poses a risk to the integrity of the active layers in iOPVs, thereby imposing a significant stability limitation on OSCs configured in direct setups. Despite these drawbacks, PEDOT:PSS is still used thanks to its excellent electrical conductivity properties [55]. Herein, we examined the impact of a PEDOT:PSS as HTL on the performance of binary and ternary iOPVs using three ETL materials with different thicknesses as shown in Figure 6a. The iOPV device layers are based on the same thicknesses as previously, with the WO_3 HTL material replaced by PEDOT:PSS. The increase in photovoltaic parameters observed in ternary devices incorporating PEDOT:PSS as the HTL exceeded that of binary devices, irrespective of material or ETL thickness as seen in Figures 6b–6e. Interestingly, the photovoltaic parameter results highlight that iOPV devices with SnO_2 ETL present the lowest performance as ETL thickness increases, in contrast to TiO_2- and ZnO-based iOPV devices. In Figure 6d, there is a

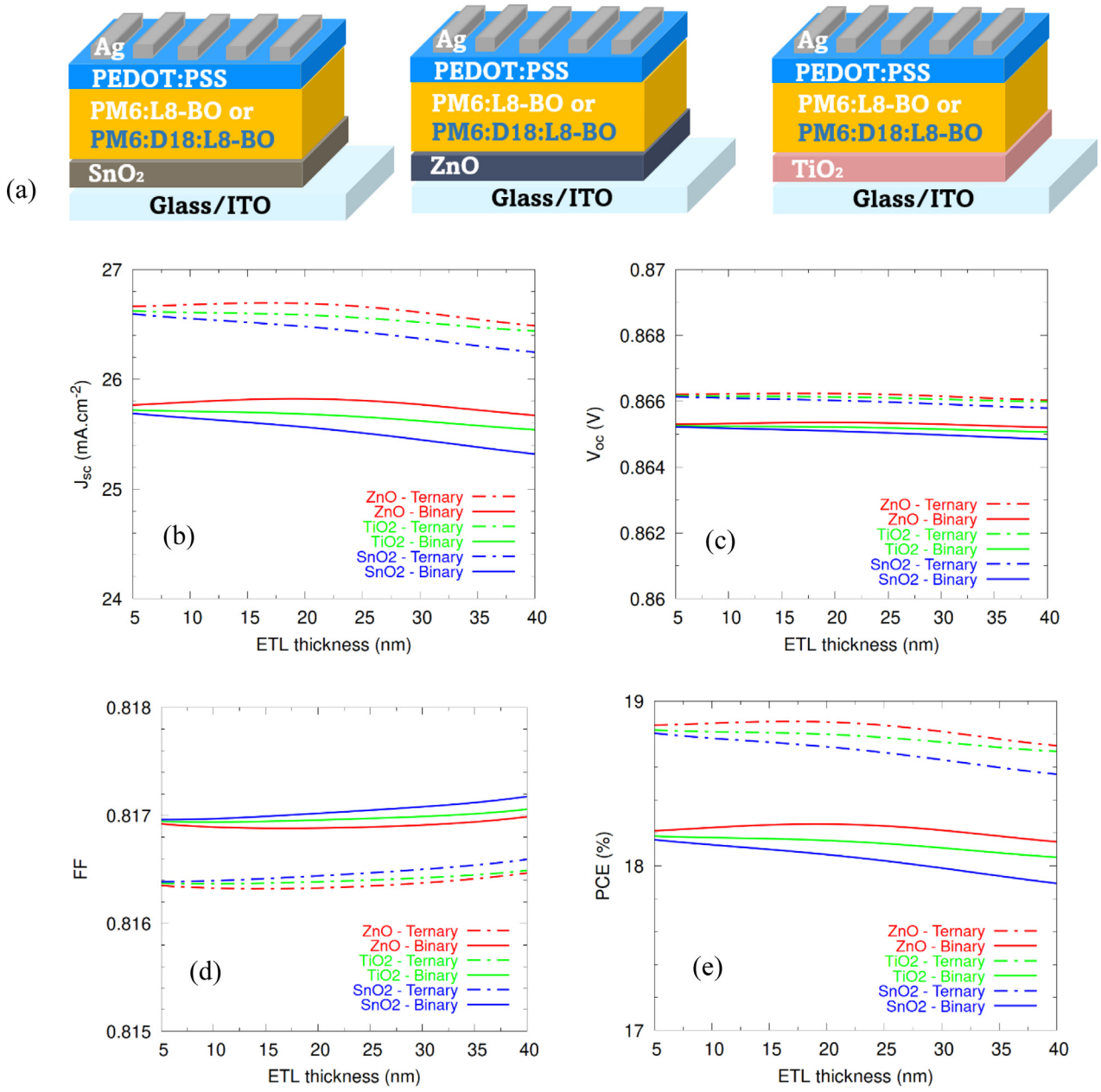

Fig. 6. (a) Schematic of the simulated iOPVs based on binary and ternary blends using different ETL materials with PEDOT:PSS as HTL. Variations of iOPV device performance parameters with different thicknesses and materials of ETL: (b) J_{sc}, (c) V_{oc}, (d) FF, and (e) PCE.

marginal improvement in FF results with increasing ETL thicknesses, particularly with the SnO_2 ETL, which surpasses the other two ETLs. However, as with the other ETLs, the differences between FF and V_{oc} are minimal. An optimal PCE of 18.88% is achieved by the ternary iOPV with 17 nm thick ZnO ETL, thanks to the enhancement of J_{sc} (26.69 mA.cm^{-2}). The V_{oc} is 0.866 V and FF 0.8163. Similarly, the binary iOPV devices show the highest PCE of 18.25% with a 19 nm thick ZnO ETL, yielding a J_{sc} of 25.82 mA.cm^{-2}, FF of 0.8169, and V_{oc} of 0.865 V. This correlates with the observations with iOPV devices using WO_3 and MoO_3 as HTL.

These results unequivocally demonstrate that whatever the choice of three different HTL or ETL materials, ternary devices using the PM6:D18:L8-BO active layer consistently outperform their binary counterparts using the PM6:L8-BO active layer, with significantly improved J_{sc} and PCE values. For example, using a 5 nm MoO_3 HTL and SnO_2 ETL, the differences in FF and V_{oc} between the binary and ternary devices are negligible, while there is a slight 3.5% improvement in J_{sc}, leading to a similar increase in PCE, attributed to efficient exciton diffusion and reduced recombinations. In addition, the equivalent maximum PCE (18.9%) and J_{sc} (26.7 mA.cm^{-2}) can be achieved with

Table 3. Comparative analysis of electrical parameters for simulated ternary iOPVs and recent experimental ternary OPVs.

Device structure	V_{oc} (V)	J_{sc} (mA.cm^{-2})	FF	PCE (%)	References
ITO/ZnO/BHJ (D18:Y6:C60-SAM)/MoO3/Ag	0.81	24.5	0.72	15.6	[45]
ITO/PEDOT:PSS/PM6:BTPeC9:IT-4F/PDIN/Al.	0.86	27.8	76.5	18.2	[57]
ITO/PEDOT:PSS/Active layer/PDINN/Ag.	0.873	27.2	73.5	17.6	[58]
ITO/PEDOT:PSS/PM6:Y6:FPDI-2PD /PFN-Br/Ag	0.848	27.47	77.20	18.00	[59]
ITO/PEDOT:PSS/PM6:Y6:BTP-PIO/PDINN/Ag,	0.848	27.31	73.9	17.10	[60]
ITO/PEDOT:PSS/PM6:m-BTP-PhC6:Qx2/PNDIT-F3N/Ag	0.871	26.71	80.04	18.62	[61]
ITO/ZnO/PM6:D18:L8-BO /MoO3/Ag	0.866	26.72	81.62	18.89	This work

various thickness combinations of ZnO and HTL materials. For example, using 15 nm ZnO with a MoO_3 HTL, or 14 nm ZnO with WO_3, or 17 nm ZnO with PEDOT:PSS, all give almost identical PCE and J_{sc} values. This demonstrates that MoO_3 or WO_3 materials can be utilized as viable alternatives to PEDOT:PSS because they provide similar device performance while potentially delivering other advantages in terms of availability, stability, and compatibility with the existing fabrication process. In ternary devices, employing ZnO as the ETL consistently yields the highest J_{sc} and PCE values for thicknesses below 33 nm. However, this study also indicates that iOPV devices with TiO_2 or SnO_2 ETL can be competitive with those with ZnO ETL at the finest thicknesses, offering a viable alternative to the ZnO ETL material widely used in the fabrication of iOPV devices. This is particularly important given that ZnO is known to exhibit poor stability when exposed to UV light, and possesses photocatalytic activity, which can accelerate the degradation of the active layer [56]. A 5 nm-thick SnO_2 ETL, when using a MoO_3 or WO_3 HTL, yields a PCE of 18.84% compared to the 18.89% obtained with a 5 nm-thick ZnO ETL. This minor difference prompts consideration of the balance between performance and other material characteristics. In Table 3, we compared the electrical parameters of our simulated iOPV with those of recent experimental OPV devices. For instance, our device achieves a V_{oc} of 0.866 V, a J_{sc} of 26.72 mA.cm^{-2}, an FF of 81.62%, and a PCE of 18.89%. This performance is competitive with several state-of-the-art experimental results. For example, the device reported by Liu et al. [59] shows a PCE of 18%, and the device by Wang et al. [61] achieves a PCE of 18.62%. Our simulated OPV matches closely with these experimental values, showcasing the robustness of our simulation approach. Additionally, our FF of 81.62% is one of the highest reported, indicating efficient charge collection and minimal recombination losses. Compared to the inverted structure device by Jeong et al. [45] with a PCE of 15%, our device shows significantly improved performance metrics. Additionally, our J_{sc} value of 26.72 mA.cm^{-2} is comparable to those reported by other researchers, further validating our methodology. This comparison demonstrates that our simulated iOPVs are on par with, or even superior to, many current experimental devices. It underscores the potential and reliability of our simulation techniques for optimizing OPV performance.

Ultimately, the present numerical study proposes an effective approach to improving the performance of iOPV devices using a thin ETL film with a targeted thickness of around 15 ± 2 nm, achievable using the atomic layer deposition (ALD) technique. Di Mario et al. [62] recently reported on the proposed strategy in which iOPV devices fabricated with the structure ITO/ALD-SnO_2/PM6:L8-BO active layer/MoOx/Al, using a 12 nm-thick SnO_2 film as the ETL deposited via ALD, achieved higher overall performance than those based on ZnO.

3.5 Study implications and limitations

Our study underscores the potential for enhancing PCE in commercial OPV applications through the optimization of layer thicknesses. This optimization not only promises more cost-effective manufacturing but also advances flexible and lightweight photovoltaic technologies. By demonstrating the critical influence of layer thickness on device performance, the study contributes to the ongoing development of sustainable energy solutions, effectively addressing various needs in the renewable energy sector.

However, the study faces several limitations. Firstly, there is a significant reliance on simulation data, which may not accurately replicate real-world conditions or account for all factors affecting OPV performance. Additionally, variability in material properties could introduce uncertainties that impact the reliability of the outcomes. Despite the

robustness of the computational models, inherent limitations exist. Therefore, experimental validation is crucial to confirm the simulated results and ensure their practical relevance and applicability in real-world scenarios.

3.6 Future research directions

To advance OPV technology, future efforts will focus on several key areas. (i) Exploring new donor and acceptor materials by synthesizing and characterizing those with improved optoelectronic properties to boost efficiency and stability. (ii) Optimizing blend ratios in ternary systems to enhance charge generation and transport efficiencies. (iii) Developing more efficient charge transport layers by engineering and characterizing inverted OPV devices, optimizing electron and hole transport layers, precisely controlling layer thicknesses, and assessing long-term stability under various environmental conditions. (iv) Conducting theoretical investigations into advanced material combinations and device architectures using computational modeling to push OPV performance limits, aiming for higher PCEs and improved durability, ultimately aiding in their practical deployment in renewable energy applications. (v) Integrating insights with OghmaNano to further enhance understanding of charge transport mechanisms. This approach provides a comprehensive multiscale description by leveraging the strengths of each computational method mentioned in Section 2, particularly for modeling disordered materials like organic semiconductors, through the combination of drift-diffusion modeling and effective medium approximation for detailed and efficient OPV device simulations.

4 Conclusion

In the present study, we utilized OghmaNano software to investigate the impact of charge transport layers on the efficiency of inverted organic photovoltaic (iOPV) devices. The study involved the analysis of three electron transport layers (ETLs) such as ZnO, TiO_2, and SnO_2 – as well as three-hole transport layers (HTLs) namely MoO_3, WO_3, and PEDOT:PSS for binary systems (PM6:L8-BO) and ternary photoactive layers (PM6:D18:L8-BO). Our study revealed that a photoactive layer thickness of 80 nm, combined with a 15 nm-thick ZnO layer and MoO_3 HTL, achieves a maximum efficiency of 18.89% in ternary devices due to ZnO's advantageous properties and the effectiveness of the ternary blending approach. Further investigation of ETL thicknesses for each HTL, on binary and ternary active layers, highlighted the advantages of ternary materials. Specifically, we observed that various combinations of ZnO thicknesses and HTL materials gave almost identical PCE and J_{sc} values, offering flexibility in HTL selection. Notably, using ZnO as ETL consistently produced the highest J_{sc} and PCE values for thicknesses below 33 nm in ternary devices. Additionally, our studies found that iOPVs devices with TiO_2 or SnO_2 ETL might rival in comparison with ZnO ETL, especially at tiny thicknesses, indicating new device manufacturing choices. Overall, our findings recommend the adoption of a thin ETL layer, roughly 15 ± 2 nm thick, to improve iOPVs device performance. Lastly, this work demonstrates the ability of thin ETLs to deliver exceptional performance in inverted OPVs.

Funding

The APC was funded via the National Open Access agreement signed by the University of Lille.

Conflicts of interest

The authors have nothing to disclose.

Data availability statement

The generated data are available upon request to the corresponding author.

Author contribution statement

Kekeli N'Konou supervised the study and simulations were carried out by Vincent Magnin. Both authors contributed to the preparation of the figures and to the redaction of the paper and have approved the final manuscript.

Supplementary material

Figure S1. Screenshots from the OghmaNano software interface, illustrating electrical parameters for the active layers, (binary on the left and ternary on the right).
Figure S2. Example of raw results (dots) obtained with OghmaNano ((a) PCE on the left and (b) J_{sc} on the right) fitted by fourth-degree polynomials (thick lines). The simulated iOPVs have a binary blend, a ZnO ETL, and a MoO_3 HTL.

The Supplementary material is available at https://www.epj-pv.org/10.1051/epjpv/2024024/olm.

References

1. X. Li, H. Ke, S. Li, M. Gao, S. Li, J. Yu, H. Xie, K. Zhou, K. Zhang, L. Ye, Intrinsically stretchable organic photovoltaic cells with improved mechanical durability and stability via dual-donor polymer blending, Adv. Funct. Mater., **34**, 2400702 (2024). https://doi.org/10.1002/adfm.202400702
2. D. Müller, E. Jiang, L. Campos Guzmán, P. Rivas Lázaro, C. Baretzky, S. Bogati, B. Zimmermann, U. Würfel, Ultra-stable ITO-free organic solar cells and modules processed from non-halogenated solvents under indoor illumination, Small **20**, 2305437 (2024). https://doi.org/10.1002/smll.202305437
3. Q. Ye, Z. Chen, D. Yang, W. Song, J. Zhu, S. Yang, J. Ge, F. Chen, Z. Ge, Ductile oligomeric acceptor-modified flexible organic solar cells show excellent mechanical robustness and near 18% efficiency, Adv. Mater. **35**, 2305562 (2023). https://dx.doi.org/10.1002/adma.202305562

4. Y. Xu, H. Yao, L. Ma, Z. Wu, Y. Cui, L. Hong, Y. Zu, J. Wang, H.Y. Woo, J. Hou, Organic photovoltaic cells with high efficiencies for both indoor and outdoor applications, Mater. Chem. Front. **5**, 893 (2021). https://doi.org/10.1039/D0QM00633E
5. C. Liu, J. Liu, X. Duan, Y. Sun, Green-processed non-fullerene organic solar cells based on y-series acceptors, Adv. Sci. **10**, 2303842 (2023). https://doi.org/10.1002/advs.202303842
6. X. Kong, T. He, H. Qiu, L. Zhan, S. Yin, Progress in organic photovoltaics based on green solvents: from solubility enhancement to morphology optimization, Chem. Commun. **59**, 12051 (2023). https://doi.org/10.1039/D3CC04412B
7. F.J. Zhang, D.W. Zhao, Z.L. Zhuo, H. Wang, Z. Xu, Y.S. Wang, Inverted small molecule organic solar cells with Ca modified ITO as cathode and MoO_3 modified Ag as anode, Sol. Energy Mater. Sol. Cells **94**, 2416 (2010). https://doi-org.insis.bib.cnrs.fr/10.1016/j.solmat.2010.08.031
8. S. Savagatrup, A.D. Printz, T.F. O'Connor, A.V. Zaretski, D. Rodriquez, E.J. Sawyer, K.M. Rajan, R.I. Acosta, S.E. Root, D. J. Lipomi, Mechanical degradation and stability of organic solar cells: molecular and microstructural determinants, Energy Environ. Sci. **8**, 55 (2014). https://doi.org/10.1039/C4EE02657H
9. W. Li, D. Liu, T. Wang, Stability of non-fullerene electron acceptors and their photovoltaic devices, Adv. Funct. Mater. **31**, 2104552 (2021). https://doi.org/10.1002/adfm.202104552
10. E.M. Speller, A.J. Clarke, J. Luke, H.K.H. Lee, J.R. Durrant, N. Li, T. Wang, H.C. Wong, J.-S. Kim, W.C. Tsoi, Z. Li, J. Mater. Chem. A **7**, 23361 (2019). https://doi.org/10.1039/C9TA05235F
11. P. Ding, D. Yang, S. Yanga, Z. Ge, Stability of organic solar cells: toward commercial applications, Chem. Soc. Rev. **53**, 2350 (2024). https://dx.doi.org/10.1039/d3cs00492a
12. Z. Chen, J. Zhu, D. Yang, W. Song, J. Shi, J. Ge, Y. Guo, X. Tong, F. Chen, Z. Ge, Isomerization strategy on non-fullerene guest acceptor enables stable organic solar cells over 19% efficiency, Energy Environ. Sci. **16**, 3119 (2023). https://dx.doi.org/10.1039/d3ee01164j
13. T. Lin, T. Dai, Double cathode modification improves charge transport and stability of organic solar cells, Energies **15**, 7643 (2022). https://doi.org/10.3390/en15207643
14. S. K. Gupta, A. Shah, D.P. Singh, Chapter 19 – Metal oxides in organic solar cells, in *Metal Oxides for Next-Generation Optoelectronic, Photonic, and Photovoltaic Applications* (Elsevier, Amsterdam, 2024), pp. 577–606. https://doi.org/10.1016/b978-0-323-99143-8.00018-3
15. H. Zheng, D. Zhou, L. Hu, Z. Xu, H. Xu, Y. Zhang, Y. Tong, B. Hu, Z. Li, L. Chen, Passivating the defects and modulating the surface energy of ZnO cathode interlayer for efficient nonfullerene organic solar cells, Sol. RRL **6**, 2200871 (2022). https://doi.org/10.1002/solr.202200871
16. S. Trost, T. Becker, A. Polywka, P. Görrn, M.F. Oszajca, N.A. Luechinger, D. Rogalla, M. Weidner, P. Reckers, T. Mayer, T. Riedl, Avoiding photoinduced shunts in organic solar cells by the use of tin oxide (SnO_x) as electron extraction material instead of ZnO, Adv. Energy Mater. **6**, 1600347 (2016). https://doi.org/10.1002/aenm.201600347
17. G.K. Dalapati, H. Sharma, A. Guchhait, N. Chakrabarty, P. Bamola, Q. Liu, G. Saianand, A.M. Sai Krishna, S. Mukhopadhyay, A. Dey, T.K.S. Wong, S. Zhuk, S. Ghosh, S. Chakrabortty, C. Mahata, S. Biring, A. Kumar, C.S. Ribeiro, S. Ramakrishna, A.K. Chakraborty, S. Krishnamurthy, P. Sonar, M. Sharma, Tin oxide for optoelectronic, photovoltaic and energy storage devices: a review, J. Mater. Chem. A **9**, 16621 (2021). https://doi.org/10.1039/d1ta01291f
18. S. Shin, S. Shafian, K.Y. Ryu, Y.-K. Jeon, W.-S. Kim, K. Kim, Solution-processed TiO_2 nanoparticles functionalized with catechol derivatives as electron transporting layer materials for organic photovoltaics, Adv. Mater. Interfaces **9**, 2200118 (2022). https://doi.org/10.1002/admi.202200118
19. D.K. Chaudhary, P.K. Dhawan, S.P. Patel, H.P. Bhasker, Large area semitransparent inverted organic solar cells with enhanced operational stability using TiO_2 electron transport layer for building integrated photovoltaic devices, Mater. Lett. **283**, 128725 (2021). https://doi.org/10.1016/j.matlet.2020.128725
20. D.A. Mengistie, M.A. Ibrahem, P.C. Wang, C.W. Chu, Highly conductive PEDOT:PSS treated with formic acid for ITO-free polymer solar cells, ACS Appl. Mater. Interfaces **6**, 2290 (2014). https://doi.org/10.1021/am405024d
21. L.Y. Yin, Z.X. Zhao, F.Y. Jiang, Z.F. Li, S.X. Xiong, Y.H. Zhou, PEDOT:PSS top electrode prepared by transfer lamination using plastic wrap as the transfer medium for organic solar cells, Org. Electron. **15**, 2593 (2014). https://doi-org.insis.bib.cnrs.fr/10.1016/j.orgel.2014.07.028
22. S. Guan, Y. Li, C. Xu, N. Yin, C. Xu, C. Wang, M. Wang, Y. Xu, Q. Chen, D. Wang, L. Zuo, H. Chen, Self-assembled interlayer enables high-performance organic photovoltaics with power conversion efficiency exceeding 20%, Adv. Mater., **36**, 2400342 (2024). https://doi.org/10.1002/adma.202400342
23. Y. Jiang, S. Sun, R. Xu, F. Liu, X. Miao, G. Ran, K. Liu, Y. Yi, W. Zhang, X. Zhu, Non-fullerene acceptor with asymmetric structure and phenyl-substituted alkyl side chain for 20.2% efficiency organic solar cells, Nat. Energy, **9**, 975 (2024). https://doi.org/10.1038/s41560-024-01557-z
24. W. Zhang, Y. Yue, R. Yang, Y. Zhang, W. Du, G. Lu, J. Zhang, H. Zhou, X. Zhang, Y. Zhang, A high-efficiency and stable organic solar cell with balanced crystallization kinetics, Energy Environ. Sci. **17**, 2182 (2024). https://doi.org/10.1039/D3EE04169G
25. J. Fu, Q. Yang, P. Huang, S. Chung, K. Cho, Z. Kan, H. Liu, X. Lu, Y. Lang, H. Lai, F. He, P.W.K. Fong, S. Lu, Y. Yang, Z. Xiao, G. Li, Rational molecular and device design enables organic solar cells approaching 20% efficiency, Nat. Commun. **15**, 1830 (2024). https://doi.org/10.1038/s41467-024-46022-3
26. X. Yu, P. Ding, D. Yang, P. Yan, H. Wang, S. Yang, J. Wu, Z. Wang, H. Sun, Z. Chen, L. Xie, Z. Ge, Self-assembled molecules with asymmetric backbone for highly stable binary organic solar cells with 19.7% efficiency, Angew. Chem. Int. Ed. **63**, e202401518 (2024). https://doi.org/10.1002/anie.202401518
27. N.Y. Doumon, L. Yang, F. Rosei, Ternary organic solar cells: A review of the role of the third element, Nano Energy **94**, 106915 (2022). https://doi.org/10.1016/j.nanoen.2021.106915

28. D.H. Kim, D.J. Lee, B. Kim, C. Yun, M.H. Kang, Tailoring PEDOT:PSS polymer electrode for solution-processed inverted organic solar cells, Solid-State Electron. **169**, 107808 (2020). https://doi.org/10.1016/j.sse.2020.107808
29. S. Wang, Simulation and optimization of C60-based organic light-emitting diodes, Mater. Sci. Forum **1026**, 142 (2021). https://doi.org/10.4028/www.scientific.net/MSF.1026.142
30. T. Tharun, A. Manimegala, A. Vasantharthan, N. Vinitha, M. Shenbagapriya, Optimization of layer thickness of htl free perovskite solar cell, i-Manager's J. Mater. Sci. **8**, 31 (2021). https://doi.org/10.26634/jms.8.4.17536
31. R.C.I. MacKenzie, T. Kirchartz, G.F.A. Dibb, J. Nelson, Modeling nongeminate recombination in P3HT:PCBM solar cells, J. Phys. Chem. C **115**, 9806 (2011). https://doi.org/10.1021/jp200234m
32. A. Singh, A. Pande, D. Patwa, R. Kalaria, A. Jain, A. Kumar, N. Gupta, OghmaNano simulation of PM6:D18:L8-BO organic solar cell and comparison with other lesser efficient solar cells, in *2023 4th International Conference for Emerging Technology (INCET)*, (Belgaum, India, 2023), pp. 1–4. https://doi.org/10.1109/INCET57972.2023.10170292
33. M. Omrani, H. Fallah, K.-L. Choy, M. Abdi-Jalebi, Impact of hybrid plasmonic nanoparticles on the charge carrier mobility of P3HT: PCBM polymer solar cells, Sci. Rep. **11**, 19774 (2021). https://doi-org.insis.bib.cnrs.fr/10.1038/s41598-021-99095-1
34. A.K. Mishra, R.K. Shukla, Simulation of photovoltaic material (donor blends PTB7:PC70BM) polymer for solar cell application, Mater. Today: Proc. **46**, 2288 (2021). https://doi.org/10.1016/j.matpr.2021.04.084
35. M. Hußner, R.A. Pacalaj, G. Olaf Müller-Dieckert, C. Liu, Z. Zhou, N. Majeed, S. Greedy, I. Ramirez, N. Li, S. M. Hosseini, C. Uhrich, C.J. Brabec, J.R. Durrant, C. Deibel, R.C.I. MacKenzie, Machine learning for ultra high throughput screening of organic solar cells: solving the needle in the haystack problem, Adv. Energy Mater. **14**, 2303000 (2024). https://doi.org/10.1002/aenm.202303000
36. R.C.I. MacKenzie, T. Kirchartz, G.F.A. Dibb, J. Nelson, Modeling nongeminate recombination in P3HT:PCBM solar cells, J. Phys. Chem. C **115**, 9806 (2011). https://doi.org/10.1021/jp200234m
37. R.C.I. MacKenzie, C.G. Shuttle, M.L. Chabinyc, J. Nelson, Extracting microscopic device parameters from transient photocurrent measurements of P3HT:PCBM solar cells, Adv. Energy Mater. **2**, 662 (2012). https://doi.org/10.1002/aenm.201100709
38. M. Amir, M.P. Singh, Extraction of charge transfer states dissociation probability and localized states parameters for PTB7-Th:PC71BM photovoltaic cells: using experimental J-V curves, Eng. Res. Express **6**, 015085 (2024). https://doi.org/10.1088/2631-8695/ad2488
39. K.W. Lee, K.M. Kim, J. Lee, R. Amin, B. Kim, S.K. Park, S.K. Lee, S. H. Park, H. J. Kim, A two-dimensional DNA lattice implanted polymer solar cell, Nanotechnology **22**, 375202 (2011). https://doi.org/10.1088/0957-4484/22/37/375202
40. J.-C. Wang, W.-T. Weng, M.-Y. Tsai, M.-K. Lee, S.-F. Horng, T.-P. Perng, C.-C. Kei, C.-C. Yuc, H.-F. Mengd, Highly efficient flexible inverted organic solar cells using atomic layer deposited ZnO as electron selective layer, J. Mater. Chem. **20**, 862 (2010). https://doi.org/10.1039/B921396A
41. T.-Y. Tsai, P.-R. Yan, S.-H. Yang, Solution-processed hybrid light-emitting devices comprising TiO_2 nanorods and WO_3 layers as carrier-transporting layers, Nanoscale Res. Lett. **11**, 516 (2016). https://doi.org/10.1186/s11671-016-1733-x
42. L. Zhu, M. Zhang, J. Xu, C. Li, J. Yan, G. Zhou, W. Zhong, T. Hao, J. Song, X. Xue, Z. Zhou, R. Zeng, H. Zhu, C.-C. Chen, R.C.I. MacKenzie, Y. Zou, J. Nelson, Y. Zhang, Y. Sun, F. Liu, Single-junction organic solar cells with over 19% efficiency enabled by a refined double-fibril network morphology, Nat. Mater. **21**, 656 (2022). https://doi.org/10.1038/s41563-022-01244-y
43. V.-H. Tran, R.B. Ambade, S.B. Ambade, S.-H. Lee, I.-H. Lee, Low-Temperature Solution-Processed SnO_2 Nanoparticles as a Cathode Buffer Layer for Inverted Organic Solar Cells, ACS Appl. Mater. Interfaces **9**, 1645 (2017). https://doi.org/10.1021/acsami.6b10857
44. H. Hwang, D.H. Sin, C. Park, K. Cho, Ternary organic solar cells based on a wide-bandgap polymer with enhanced power conversion efficiencies, Sci. Rep. **9**, 12081 (2019). https://doi.org/10.1038/s41598-019-48306-x
45. S. Jeong, A. Rana, J.-H. Kim, D. Qian, K. Park, J.-H. Jang, J. Luke, S. Kwon, J. Kim, P. S. Tuladhar, J.-S. Kim, K. Lee, J. R. Durrant, H. Kang, New ternary blend strategy based on a vertically self-assembled passivation layer enabling efficient and photostable inverted organic solar cells, Adv. Sci. **10**, 2206802 (2023). https://doi.org/10.1002/advs.202206802
46. Z. Liu, L. Wang, H. Zhao, P. Chen, X. Xie, High-performance inverted ternary organic solar cells using solution-processed tin oxide as the electron transport layer, Org. Electron. **120**, 106828 (2023). https://doi.org/10.1016/j.orgel.2023.106828
47. Y.-F. Liu, S.-W. Zhang, Y.-X. Li, S.-L. Li, L.-Q. Huang, Y.-N. Jing, Q. Cheng, L.-G. Xiao, B.-X. Wang, B. Han, J.J. Kang, Y. Zhang, H. Zhang, H.-Q. Zhou, Solution-processed molybdenum oxide hole transport layer stabilizes organic solar cells, Chin. J. Polym. Sci. **41**, 202 (2023). https://doi.org/10.1007/s10118-022-2873-3
48. H.-C. Cha, C.-F. Li, T.-Y. Chung, W.-Y. Ma, C.-S. Tsao, Y.-C. Huang, Spray-coated MoO3 hole transport layer for inverted organic photovoltaics, Polymers **16**, 981 (2024). https://doi.org/10.3390/polym16070981
49. S. Park, F.T.A. Wibowo, N.V. Krishna, J. Ryu, H. Lee, J.H. Lee, Y.J. Yoon, J.Y. Kim, J.H. Seo, S.-H. Oh, S.-Y. Jang, S. Cho, Importance of interface engineering between the hole transport layer and the indium-tin-oxide electrode for highly efficient polymer solar cells, J. Mater. Chem. A **9**, 15394 (2021). https://doi.org/10.1039/d1ta04078b
50. A.U. Rahman, A. El Astal-Quirós, G. Susanna, H. Javanbakht, E. Calabrò, G. Polino, B. Paci, A. Generosi, F.R. Riva, F. Brunetti, A. Reale, Scaling-up of solution-processable tungsten trioxide (WO_3) nanoparticles as a hole transport layer in inverted organic photovoltaics, Energies **17**, 814 (2024). https://doi.org/10.3390/en17040814
51. T. Matsumoto, T. Murakami, F. Schlüter, H. Murata, V. Vohra, F. Rizzo, Water-soluble organic dyes as efficient anode interlayer materials for PEDOT:PSS-free inverted bulk heterojunction solar cells, Sol. RRL **6**, 2100661 (2022). https://doi.org/10.1002/solr.202100661
52. C. Anrango-Camacho, K. Pavón-Ipiales, B.A. Frontana-Uribe, A. Palma-Cando, Recent advances in hole-transporting layers for organic solar cells, Nanomaterials **12**, 443 (2022). https://doi.org/10.3390/nano12030443

53. K. N'Konou, M. Chalh, B. Lucas, S. Vedraine, P. Torchio, Improving the performance of inverted organic solar cells embedding metal-oxide layer coating silver nanoparticles deposited by e-beam evaporation method, Polym. Int. **68**, 979 (2019). https://doi.org/10.1002/pi.5789
54. K. N'Konou, M. Chalh, V. Monnier, N.P. Blanchard, Y. Chevolot, B. Lucas, S. Vedraine, P. Torchio, Impact of $Ag@SiO_2$ core-shell nanoparticles on the photoelectric current of plasmonic inverted organic solar cells, Synth. Met. **239**, 22 (2018). https://doi.org/10.1016/j.synthmet.2018.03.003
55. X. Fan, W. Nie, H. Tsai, N. Wang, H. Huang, Y. Cheng, R. Wen, L. Ma, F. Yan, Y. Xia, PEDOT:PSS for flexible and stretchable electronics: modifications, strategies, and applications, Adv. Sci. **6**, 1900813 (2019). https://doi.org/10.1002/advs.201900813
56. X. Liu, Z. Zheng, J. Wang, Y. Wang, B. Xu, S. Zhang, J. Hou, Fluidic manipulating of printable zinc oxide for flexible organic solar cells, Adv. Mater. **34**, 2106453 (2021). https://doi.org/10.1002/adma.202106453
57. Y. Zhang, T. Huang, N. Weng, Y. Chen, D. Wang, Z. Zhang, Q. Liao, J. Zhang, Efficient ternary organic solar cells with suppressed nonradiative recombination and fine-tuned morphology via IT-4F as guest acceptor, ChemSusChem, in press e202301741 (2024). https://doi.org/10.1002/cssc.202301741
58. D. Yun, S. Xuyao, S.-Y. Lee, V. V. Sharma, H. Li, S.-J. Park, Y.-H. Kim, G.-H. Kim, High efficiency of ternary blend organic solar cells with a BTP-4F/BTP-4H derivative, ACS Appl. Energy Mater. **7**, 1243 (2024). https://doi.org/10.1021/acsaem.3c02876
59. M. Liu, X. Ge, X. Jiang, D. Chen, F. Guo, S. Gao, Q. Peng, L. Zhao, Y. Zhang, 18% efficiency of ternary organic solar cells enabled by integrating a fused perylene diimide guest acceptor, Nano Energy **112**, 108501 (2023). https://doi-org.ressources-electroniques.univ-lille.fr/10.1016/j.nanoen.2023.108501
60. T. Xu, X. Zhang, S. Zhang, W. Zhang, W. Song, A fused-ring electron acceptor with phthalimide-based ending groups for efficient ternary organic solar cells, ACS Appl. Mater. Interfaces **16**, 4618 (2024). https://doi.org/10.1021/acsami.3c15503
61. M. Wang, Y. Shi, Z. Zhang, Y. Shen, M. Lv, Y. Yan, H. Zhou, J. Zhang, K. Lv, Y. Zhang, H. Penge, Z. Wei, Improving the efficiency of ternary organic solar cells by reducing energy loss, Nanoscale Horiz. **8**, 1073 (2023). https://doi.org/10.1039/D3NH00122A
62. L. Di Mario, D. Garcia Romero, H. Wang, E.K. Tekelenburg, S. Meems, T. Zaharia, G. Portale, M.A. Loi, Outstanding fill factor in inverted organic solar cells with SnO_2 by atomic layer deposition, Adv. Mater., **36**, 2301404 (2024). https://doi.org/10.1002/adma.202301404

Cite this article as: Vincent Magnin, Kekeli N'Konou, Numerical study of charge transport layers in inverted ternary organic photovoltaic cells, EPJ Photovoltaics **15**, 29 (2024)